## S1 Supplementary material for "Methods"

### S1.1 Data availability

Within the July climatological datasets from each downscaled GCM, a small number of years are missing data. These are indicated in Table S1. We assume that the omission of these years has a negligible impact on the 21-year averages that we calculate for each variable.

### S1.2 Stability and turbulence calculations

Figures S1 and S2 show that our calculations of near-surface static stability (Sect. 2.2.3) and TKE (Sect. 2.2.4) are not sensitive to the choice of the top atmospheric layer used in the calculation, as the calculations with different choices of top layer are highly correlated with the approximations using the eighth $\sigma$ layer above the surface as the top. In our TKE data, we exclude the outermost three squares of grid cells surrounding the study area from our analysis due to unrealistically high TKE values at the edges of the study area.

### S1.3 Prediction regions for sea ice regressions

In the present-day regression of $D_\theta$ versus SIC (Sect. 3.1.2), each regression model is only trained on oceanic grid cells with mean present-day SIC $> 0\,\%$ to ensure sea ice is present and mean present-day SIC $\leq 90\,\%$ because there are artefacts in the data at very high SIC values as explained in Sect. 2.2.2. When predicting future $D_\theta$ (Sect. 3.3), we similarly omit oceanic grid cells with mean present-day or future SIC $> 90\,\%$ as well as oceanic grid cells which have mean SIC $= 0\,\%$ in both the present and future periods.

### S1.4 Spatial cross-validation

Selecting the number of clusters for spatial cross-validation is a persistent challenge without a clear solution (Valavi et al., 2019). We choose five clusters in each of the plateau, escarpment, and sea ice regions to generate blocks that are large enough in size to be reasonably spatially independent of other clusters. We choose six blocks over the ice shelves for the same reason and to ensure that each major ice shelf contains the same number of clusters. In the main text, the evaluation metrics we report are cross-validated, meaning that the evaluation metric for one downscaled GCM simulation is the average result across all folds of the corresponding spatial cross-validation. In this Supplement, we also report full non-cross-validated evaluation metrics from regressions calculated on all the pertinent data (Bahn and McGill, 2013; Roberts et al., 2017; Sun et al., 2023). Furthermore, we report results for different numbers of clusters in this Supplement (Roberts et al., 2017). In general, the evaluations yield similar results upon varying the number of clusters.

**Table S1.** Years with missing July data for each variable. Variable symbols are explained in the Methods (Sect. 2.2). WS represents near-surface wind speed at the third $\sigma$ level (approximately 8 m above the surface). ZZ represents the heights of the $\sigma$ levels above the surface. The letters preceding each year indicate which downscaled GCM is missing that year's data (U = MAR-UKESM, I = MAR-IPSL, C = MAR-CNRM, M = MAR-MPI).

| Time period | $D_\theta$ | $\theta_0$ | $\theta$ |
|---|---|---|---|
| 1980–2000 | U1980, C2000 | U1980, M1989, CM2000 | C2000 |
| 2080–2100 | U2081, M2092, UICM2100 | U2081, M2092, UICM2100 | U2081, M2092, UIC2100 |
| **Time period** | **SIC** | **TKE, ZZ** | **WS** |
| 1980–2000 | C2000 | UIC2000 | UIC2000 |
| 2080–2100 | M2092, UC2100 | U2081, M2092, UICM2100 | M2092, UIC2100 |

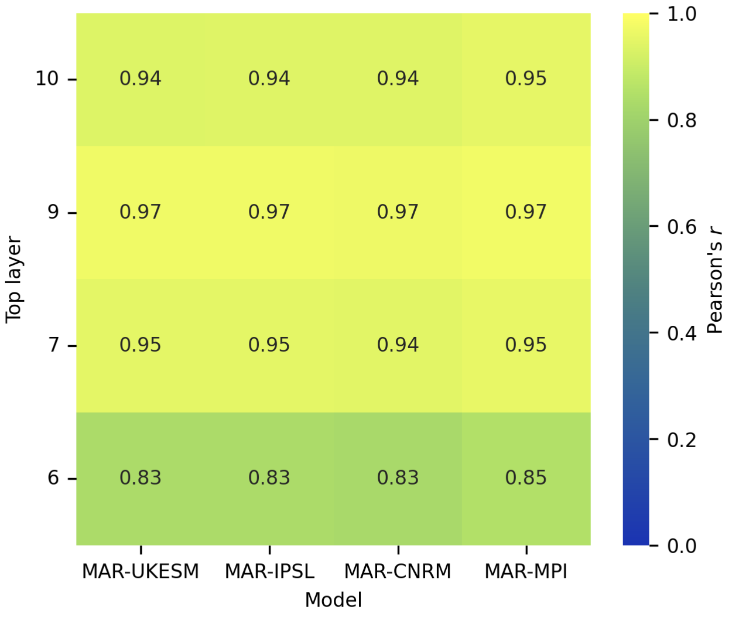


**Figure S1.** July static stability ($N^2$) estimates in the present-day period are not sensitive to the top layer choice. Heat map displaying Pearson's correlation coefficient ($r$) between the static stability estimates calculated using the eighth atmospheric layer above the surface as the top $\sigma$ layer in the calculation compared to the estimates using the sixth, seventh, ninth, and tenth atmospheric layers as the top $\sigma$ layer.

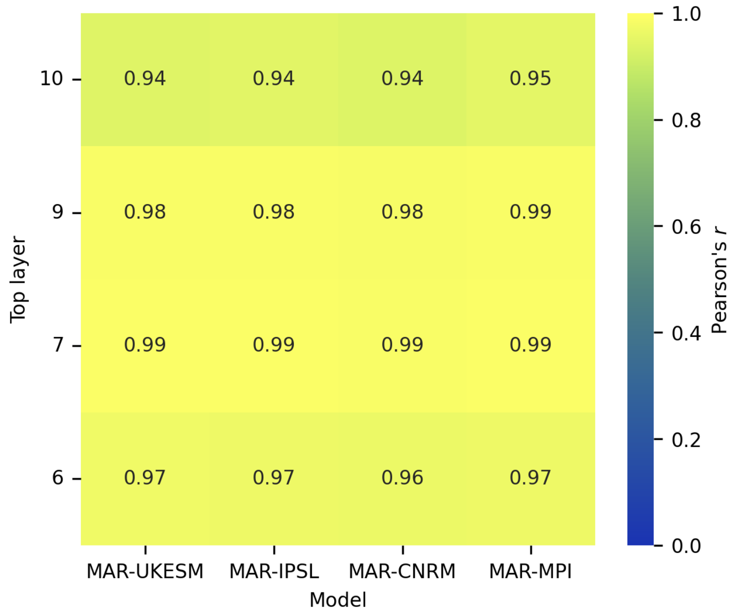


**Figure S2.** July turbulent kinetic energy (TKE) estimates in the present-day period are not sensitive to the top layer choice. Heat map displaying Pearson's correlation coefficient ($r$) between the mean surface-layer TKE estimates calculated using the eighth atmospheric layer above the surface as the top $\sigma$ layer in the calculation compared to the estimates using the sixth, seventh, ninth, and tenth atmospheric layers as the top $\sigma$ layer.

## S2 Supplementary material for "Spatial patterns in Antarctic boundary layer variables"

**Table S2.** Spearman's rank correlation coefficient ($r_s$) calculated for pairs of inversion variables by Antarctic region. $D_\theta$ is the potential temperature deficit, $N^2$ is static stability, TKE is turbulent kinetic energy, and WS is near-surface wind speed at the third $\sigma$ level (approximately $8\,\mathrm{m}$ above the surface). The spatial correlations are calculated using the mean July 1980–2000 grid cell data from the downscaled GCMs. MMM represents the multi-model mean. All correlations from each downscaled GCM are statistically significant at the 95 % significance level.

| Region | Model | $D_\theta$–$N^2$ | $D_\theta$–TKE | $N^2$–TKE | TKE–WS |
|---|---|---|---|---|---|
| Plateau | MAR-UKESM | −0.73 | 0.73 | −0.78 | 0.96 |
| | MAR-IPSL | −0.69 | 0.67 | −0.74 | 0.95 |
| | MAR-CNRM | −0.70 | 0.66 | −0.76 | 0.95 |
| | MAR-MPI | −0.71 | 0.65 | −0.76 | 0.96 |
| | MMM | −0.71 | 0.68 | −0.76 | 0.95 |
| Escarpment | MAR-UKESM | −0.55 | 0.42 | −0.69 | 0.94 |
| | MAR-IPSL | −0.54 | 0.37 | −0.67 | 0.94 |
| | MAR-CNRM | −0.57 | 0.37 | −0.67 | 0.94 |
| | MAR-MPI | −0.56 | 0.40 | −0.68 | 0.94 |
| | MMM | −0.56 | 0.39 | −0.68 | 0.94 |
| Ice shelves | MAR-UKESM | −0.89 | 0.85 | −0.88 | 0.93 |
| | MAR-IPSL | −0.90 | 0.83 | −0.88 | 0.93 |
| | MAR-CNRM | −0.88 | 0.83 | −0.88 | 0.92 |
| | MAR-MPI | −0.90 | 0.86 | −0.90 | 0.93 |
| | MMM | −0.89 | 0.84 | −0.88 | 0.93 |

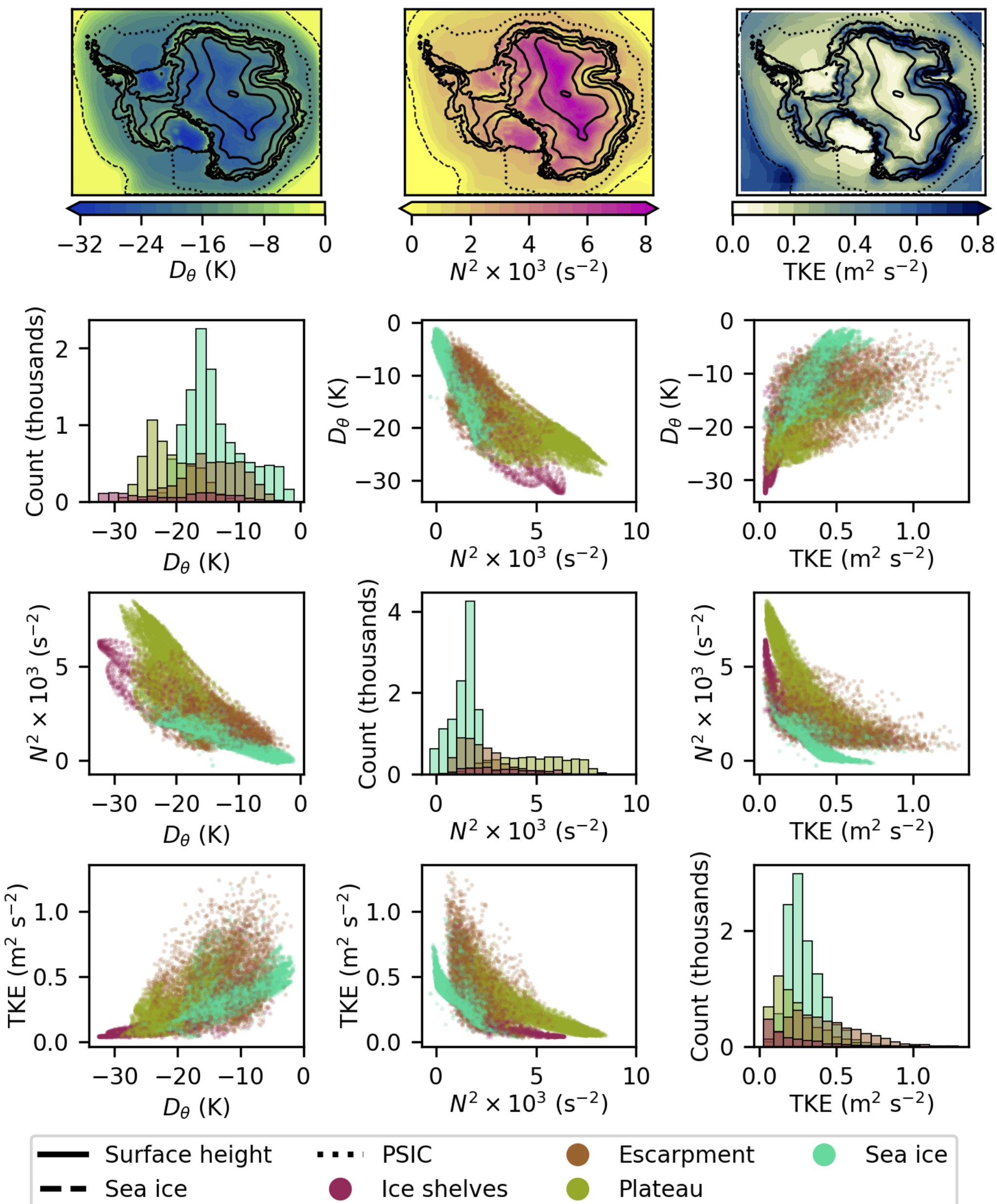


**Figure S3.** Climatology of the present-day inversion layer over Antarctica. Each data point is averaged across July 1980–2000 in MAR-UKESM. The top row depicts spatial patterns of the potential temperature deficit ($D_\theta$), static stability ($N^2$), and turbulent kinetic energy (TKE). The sea ice contour indicates the northernmost sea ice edge position for a threshold of 15 % SIC. The diagonal subplots from the second to fourth row show the distribution of grid cell values for each variable by region. The remaining subplots depict bivariate relationships for grid cell data by region.

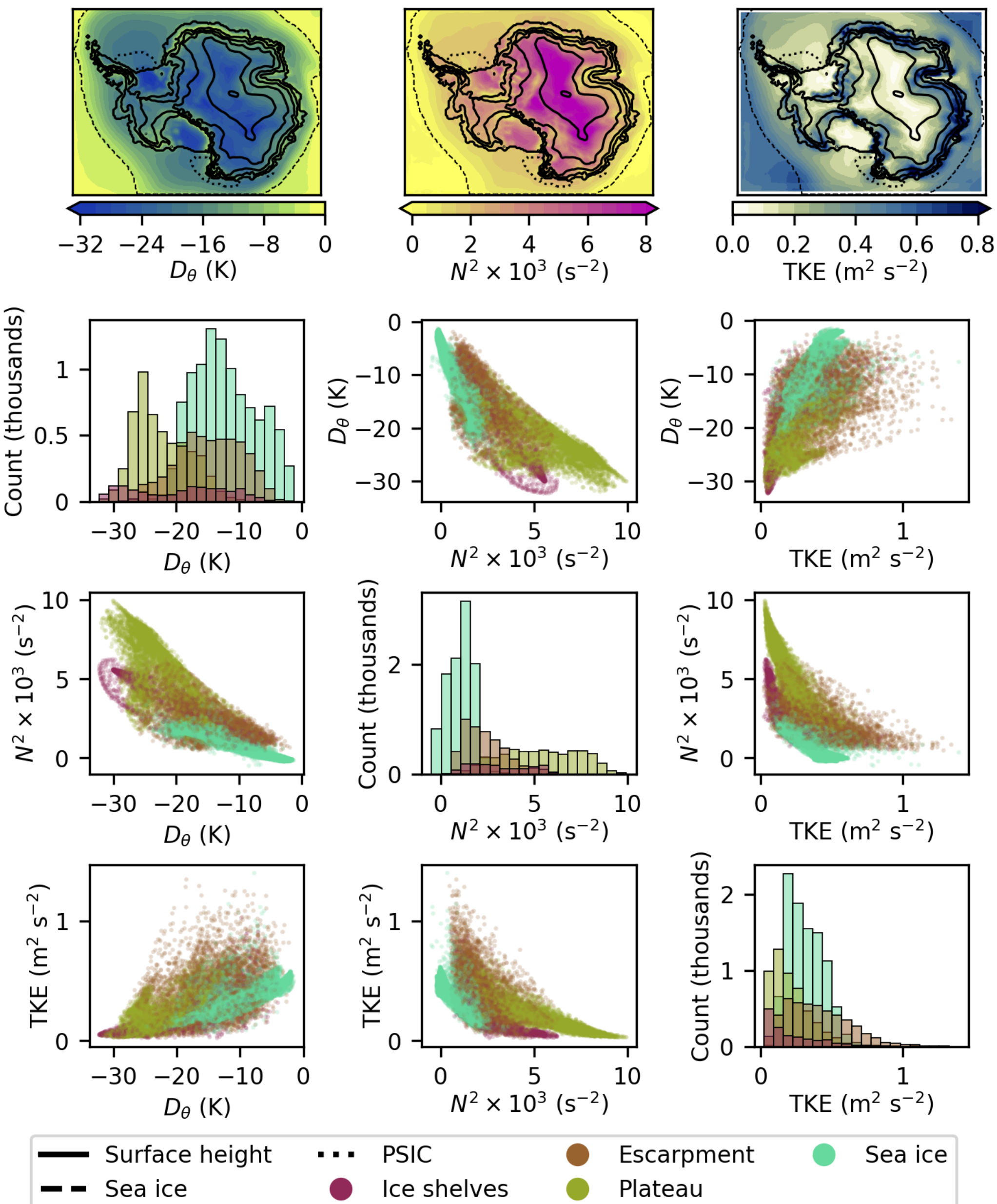


**Figure S4.** Same as Fig. S3, but for MAR-CNRM.

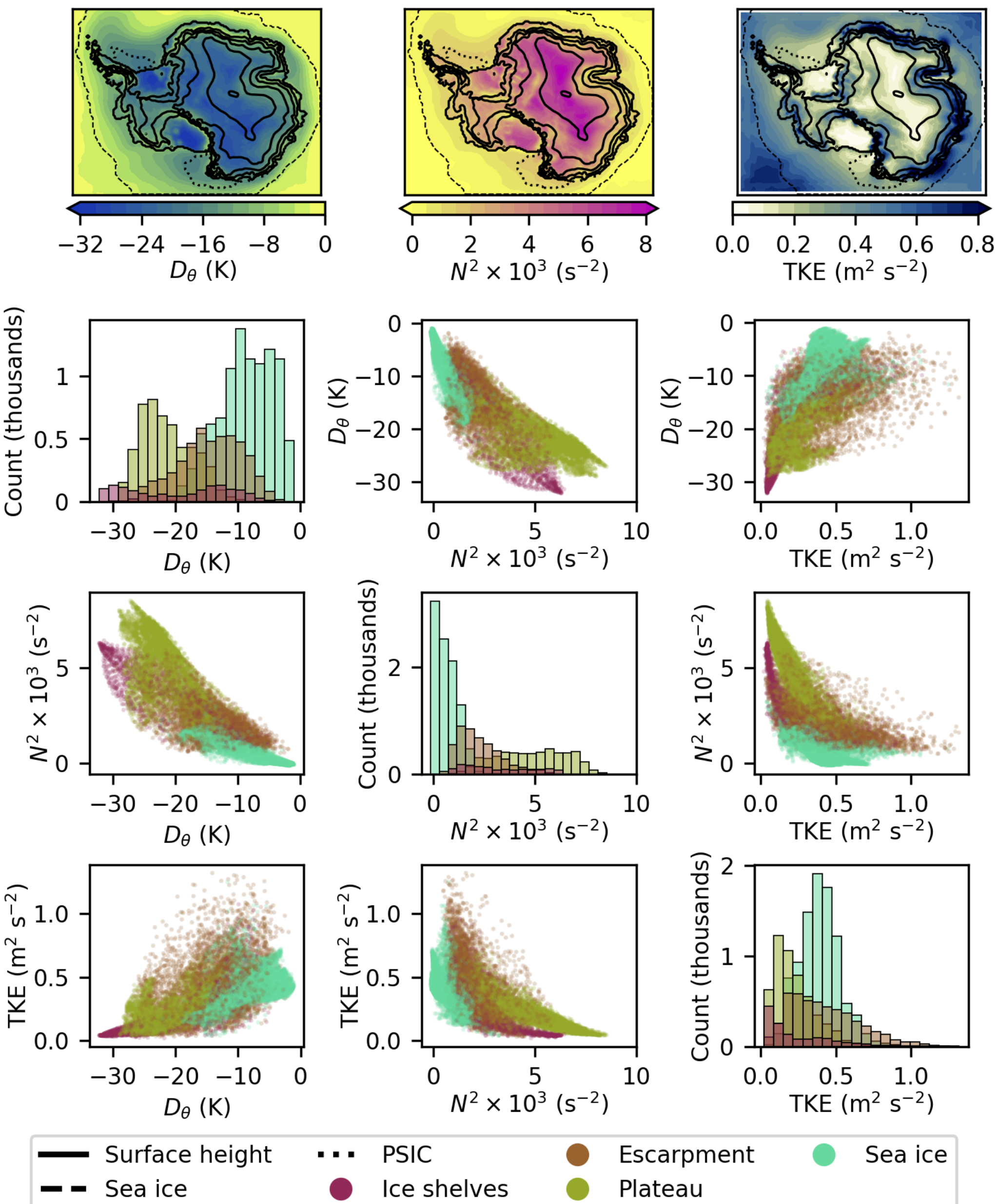


**Figure S5.** Same as Fig. S3, but for MAR-MPI.

**Table S3.** Coefficients for the quadratic regressions of the July potential temperature deficit ($D_\theta$) versus sea ice concentration (SIC) for 1980–2000. The columns correspond to the coefficients in the equation $D_\theta = a \cdot \mathrm{SIC}^2 + b \cdot \mathrm{SIC} + c$. Each coefficient from the full regression (calculated using all available data) is reported alongside the lowest and highest coefficient calculated from its corresponding five-fold spatial cross-validation in brackets.

| Model | $a$ (K %$^{-2}$) | $b$ (K %$^{-1}$) | $c$ (K) |
|---|---|---|---|
| MAR-UKESM | −0.00051 [−0.00062, −0.00043] | −0.058 [−0.066, −0.048] | −1.6 [−1.7, −1.5] |
| MAR-IPSL | −0.00065 [−0.00071, −0.00055] | −0.042 [−0.055, −0.035] | −2.0 [−2.1, −1.9] |
| MAR-CNRM | −0.00100 [−0.00104, −0.00090] | −0.019 [−0.033, −0.012] | −2.4 [−2.5, −2.2] |
| MAR-MPI | −0.00096 [−0.00105, −0.00076] | −0.022 [−0.037, −0.016] | −2.0 [−2.4, −1.9] |

**Table S4.** Model performance indicators for quadratic regression models predicting the mean July 1980–2000 potential temperature deficit ($D_\theta$) from sea ice concentration. Data are shown by the number of clusters in the spatial cross-validation and for the regressions trained on the full datasets. MAE and MAPE respectively represent mean absolute error and mean absolute percentage error.

| Clusters | Model | MAE (K) | MAPE (%) |
|---|---|---|---|
| 3 | MAR-UKESM | 1.14 | 30 |
| | MAR-IPSL | 0.93 | 20 |
| | MAR-CNRM | 1.48 | 36 |
| | MAR-MPI | 1.17 | 29 |
| 5 | MAR-UKESM | 1.20 | 29 |
| | MAR-IPSL | 1.02 | 23 |
| | MAR-CNRM | 1.34 | 30 |
| | MAR-MPI | 1.16 | 29 |
| 7 | MAR-UKESM | 1.10 | 25 |
| | MAR-IPSL | 0.98 | 21 |
| | MAR-CNRM | 1.32 | 31 |
| | MAR-MPI | 1.17 | 30 |
| Full | MAR-UKESM | 1.00 | 23 |
| | MAR-IPSL | 0.82 | 18 |
| | MAR-CNRM | 1.14 | 26 |
| | MAR-MPI | 1.07 | 25 |

## S3 Supplementary material for "Contribution of the change in inversion strength to Antarctic warming"

**Table S5.** 21st-century warming metrics in Antarctica and the surrounding ocean. Change in potential temperature ($\Delta\theta$), change in background potential temperature ($\Delta\theta_0$), change in potential temperature deficit ($\Delta D_\theta$), the contribution of $\Delta D_\theta$ to warming, and the polar amplification factor (PAF) from July 1980–2000 to July 2080–2100 averaged across each Antarctic region under SSP5-8.5. Each result is reported by downscaled GCM. $\Delta\theta$, $\Delta\theta_0$, and $\Delta D_\theta$ are statistically significant at the 95 % significance level in all the listed regions across all downscaled GCMs.

| Region | Model | $\Delta\theta$ (K) | $\Delta\theta_0$ (K) | $\Delta D_\theta$ (K) | $\Delta D_\theta$ contribution (%) | PAF |
|---|---|---|---|---|---|---|
| Plateau | MAR-UKESM | 5.9 | 5.1 | 0.9 | 14 | 0.9 |
| | MAR-IPSL | 7.9 | 6.5 | 1.5 | 17 | 1.5 |
| | MAR-CNRM | 6.6 | 5.3 | 1.4 | 19 | 1.4 |
| | MAR-MPI | 5.6 | 4.0 | 1.6 | 28 | 1.7 |
| Escarpment | MAR-UKESM | 5.7 | 5.2 | 0.6 | 9 | 0.9 |
| | MAR-IPSL | 6.1 | 5.7 | 0.5 | 7 | 1.1 |
| | MAR-CNRM | 6.3 | 5.6 | 0.7 | 10 | 1.3 |
| | MAR-MPI | 4.0 | 3.3 | 0.7 | 16 | 1.2 |
| Ice shelves | MAR-UKESM | 7.3 | 5.5 | 2.0 | 25 | 1.2 |
| | MAR-IPSL | 7.0 | 5.9 | 1.2 | 16 | 1.3 |
| | MAR-CNRM | 8.6 | 6.3 | 2.2 | 24 | 1.7 |
| | MAR-MPI | 4.8 | 3.4 | 1.4 | 26 | 1.5 |
| Sea ice | MAR-UKESM | 10.0 | 4.9 | 5.1 | 45 | 1.6 |
| | MAR-IPSL | 8.2 | 4.9 | 3.3 | 36 | 1.5 |
| | MAR-CNRM | 12.8 | 6.0 | 6.8 | 49 | 2.6 |
| | MAR-MPI | 5.4 | 3.2 | 2.2 | 34 | 1.7 |
| Continent | MAR-UKESM | 6.0 | 5.2 | 0.9 | 13 | 1.0 |
| | MAR-IPSL | 7.1 | 6.1 | 1.0 | 13 | 1.3 |
| | MAR-CNRM | 6.7 | 5.5 | 1.2 | 16 | 1.4 |
| | MAR-MPI | 4.8 | 3.7 | 1.2 | 23 | 1.5 |
| Continent+sea ice | MAR-UKESM | 8.0 | 5.0 | 3.0 | 29 | 1.3 |
| | MAR-IPSL | 7.6 | 5.5 | 2.1 | 25 | 1.4 |
| | MAR-CNRM | 9.6 | 5.7 | 3.8 | 32 | 2.0 |
| | MAR-MPI | 5.1 | 3.4 | 1.7 | 28 | 1.6 |

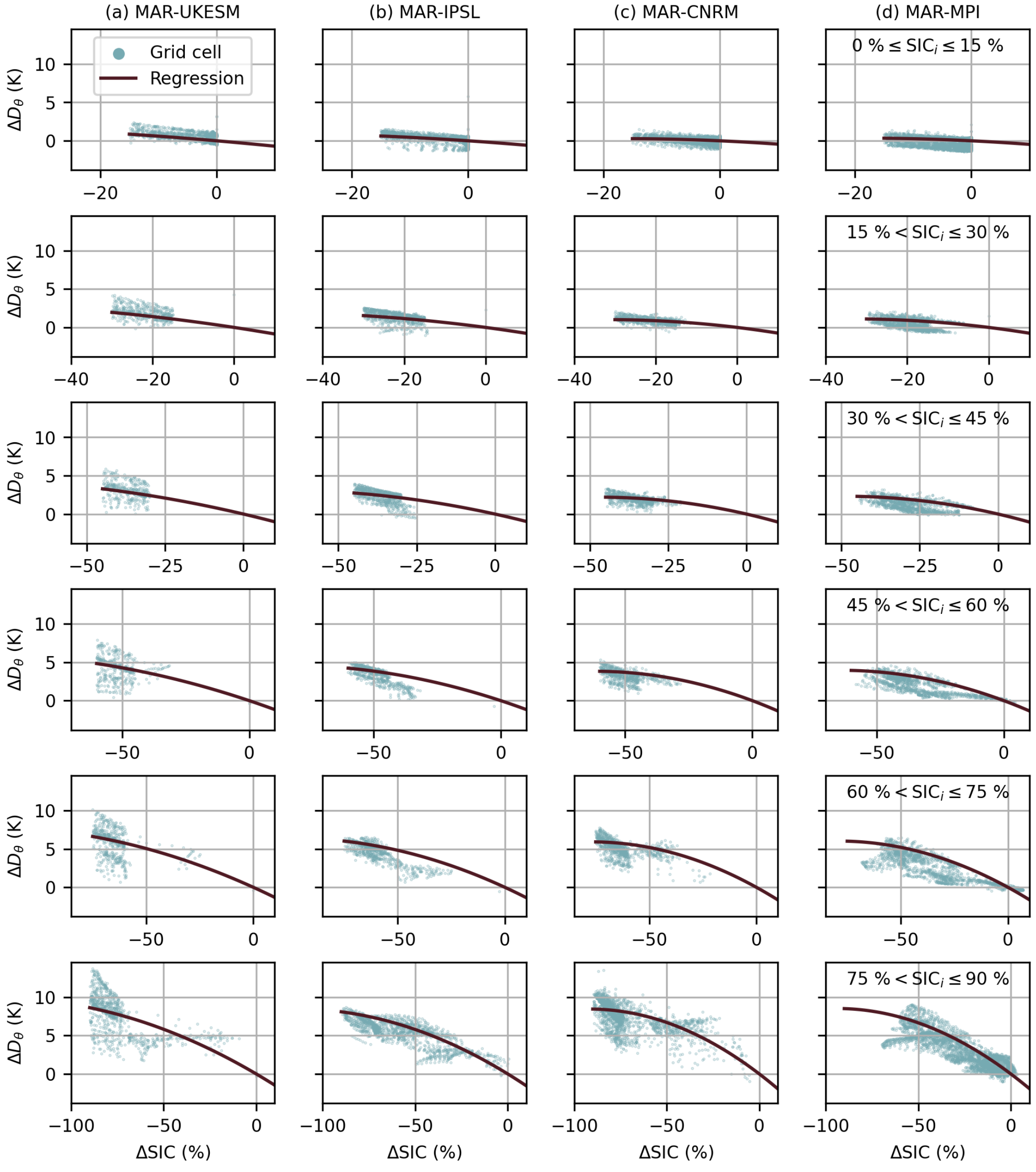


**Figure S6.** Predicting the 21st-century change in July inversion strength ($\Delta D_\theta$) from the change in sea ice concentration ($\Delta$SIC) and present-day sea ice concentration ($\mathrm{SIC}_i$). The depicted regression models are the full regressions prior to cross-validation calculated from all available data. They are derived from the present-day relationship between $D_\theta$ and SIC (Sect. 3.1.2) and are superimposed on grid cell data. In each row, only grid cell data with the mean July 1980–2000 $\mathrm{SIC}_i$ values indicated in the rightmost subplot are plotted, and that row's predictions are calculated using the mean value of the corresponding $\mathrm{SIC}_i$ range (e.g., $\mathrm{SIC}_i = 7.5\,\%$ is used to generate the regression predictions in the first row).

**Table S6.** Model performance indicators for quadratic regression models predicting the mean July 2080–2100 potential temperature deficit ($D_\theta$) from sea ice concentration. MAE and MAPE respectively represent mean absolute error and mean absolute percentage error. $D_{\theta,i}$ and $D_{\theta,f}$ represent July $D_\theta$ averaged across the prediction regions for 1980–2000 and 2080–2100, respectively. $\hat{D}_{\theta,f}$ represents future $D_\theta$ predicted from the regressions averaged across the prediction regions. Results are listed by downscaled GCM and for the multi-model mean (MMM) from the full non-cross-validated regressions calculated using all available data.

| Model | MAE (K) | MAPE (%) | $D_{\theta,i}$ (K) | $D_{\theta,f}$ (K) | $\hat{D}_{\theta,f}$ (K) |
|---|---|---|---|---|---|
| MAR-UKESM | 0.86 | 61 | −5.2 | −1.7 | −1.9 |
| MAR-IPSL | 0.67 | 26 | −5.4 | −2.9 | −2.5 |
| MAR-CNRM | 0.61 | 22 | −5.9 | −3.0 | −2.7 |
| MAR-MPI | 0.87 | 24 | −5.9 | −4.5 | −3.8 |
| MMM | 0.75 | 33 | −5.6 | −3.0 | −2.7 |

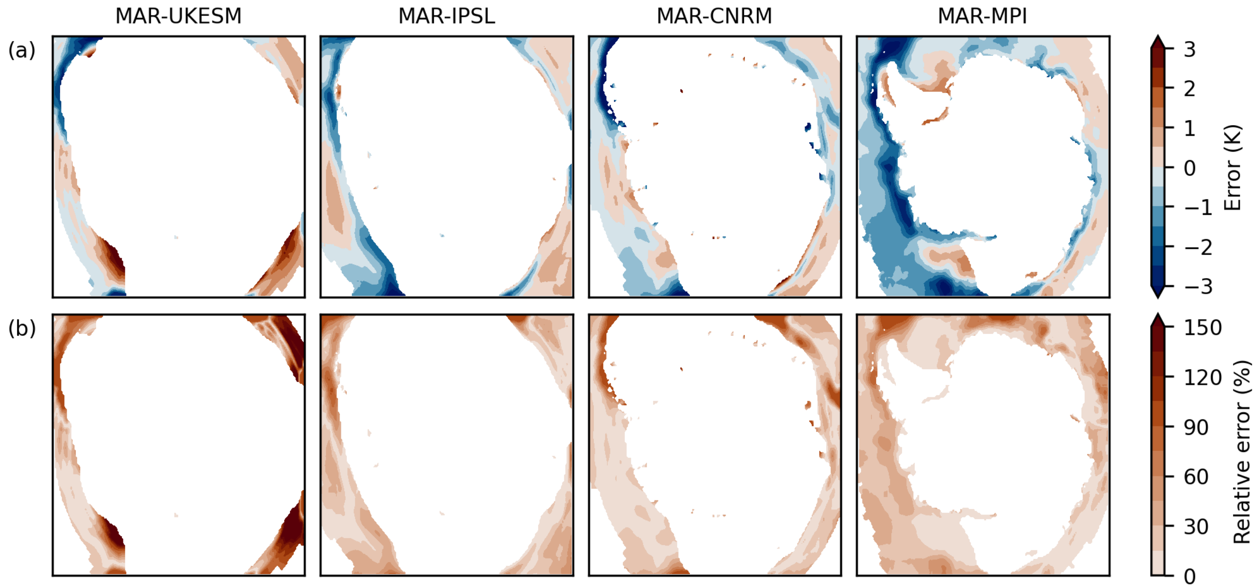


**Figure S7.** Residuals of the quadratic regression predictions of future inversion strength from sea ice concentration (SIC). (a) Error and (b) relative error for the full non-cross-validated regressions (calculated using all available data) predicting mean July 2080–2100 potential temperature deficit ($D_\theta$) from mean July 1980–2000 SIC ($SIC_i$) and the 21$^{st}$-century change in SIC ($\Delta$SIC) in the ocean surrounding Antarctica. Sect. S1.3 defines the prediction regions.

## S5 Supplementary material for "Contribution of the lapse-rate feedback to continental near-surface warming"

**Table S7.** Stronger inversions and greater atmospheric stability in the present day are associated with greater weakening of surface inversions. Spearman's rank correlation coefficient ($r_s$) is reported for the 21st-century change in inversion strength ($\Delta D_\theta$) with both the present-day inversion strength $D_\theta$ and static stability $N^2$. Results are reported by continental region and downscaled GCM. MMM represents the multi-model mean. Italics represent correlations that are not statistically significant at the 95 % significance level.

| Region | Model | $\Delta D_\theta$–$D_\theta$ | $\Delta D_\theta$–$N^2$ |
|---|---|---|---|
| Plateau | MAR-UKESM | *−0.24* | *0.17* |
| | MAR-IPSL | −0.52 | 0.49 |
| | MAR-CNRM | −0.63 | 0.61 |
| | MAR-MPI | −0.59 | 0.42 |
| | MMM | −0.50 | 0.42 |
| Escarpment | MAR-UKESM | −0.54 | 0.40 |
| | MAR-IPSL | −0.46 | 0.38 |
| | MAR-CNRM | −0.57 | 0.51 |
| | MAR-MPI | −0.75 | 0.40 |
| | MMM | −0.58 | 0.42 |
| Ice shelves | MAR-UKESM | −0.58 | 0.52 |
| | MAR-IPSL | −0.28 | 0.40 |
| | MAR-CNRM | −0.35 | 0.30 |
| | MAR-MPI | −0.66 | 0.57 |
| | MMM | −0.47 | 0.45 |

**Table S8.** Coefficients for the linear regressions of the 21st-century change in July potential temperature deficit ($\Delta D_\theta$) versus present-day July static stability ($N^2$) by region and downscaled GCM. The ice shelves region refers to the Ronne and Ross Ice Shelves. Each coefficient from the full regression (calculated using all available data) is reported alongside the lowest and highest coefficient calculated from its corresponding spatial cross-validation (five folds for the plateau and escarpment, and six folds for the ice shelves).

| Region | Model | Slope (K s$^2$) | Intercept (K) |
|---|---|---|---|
| Plateau | MAR-UKESM | 169 [143, 199] | 0.11 [−0.34, 0.23] |
| | MAR-IPSL | 305 [283, 332] | −0.12 [−0.20, −0.03] |
| | MAR-CNRM | 286 [269, 340] | −0.16 [−0.28, −0.07] |
| | MAR-MPI | 228 [216, 248] | 0.53 [0.37, 0.59] |
| Escarpment | MAR-UKESM | 211 [149, 294] | 0.13 [−0.09, 0.37] |
| | MAR-IPSL | 253 [185, 274] | −0.13 [−0.22, −0.03] |
| | MAR-CNRM | 337 [286, 369] | −0.05 [−0.25, 0.17] |
| | MAR-MPI | 343 [211, 407] | −0.03 [−0.21, 0.22] |
| Ice shelves | MAR-UKESM | 459 [434, 530] | 0.40 [0.25, 0.50] |
| | MAR-IPSL | 407 [345, 431] | −0.57 [−0.63, −0.40] |
| | MAR-CNRM | 565 [493, 657] | −0.35 [−0.78, −0.05] |
| | MAR-MPI | 315 [247, 443] | 0.38 [−0.35, 0.95] |

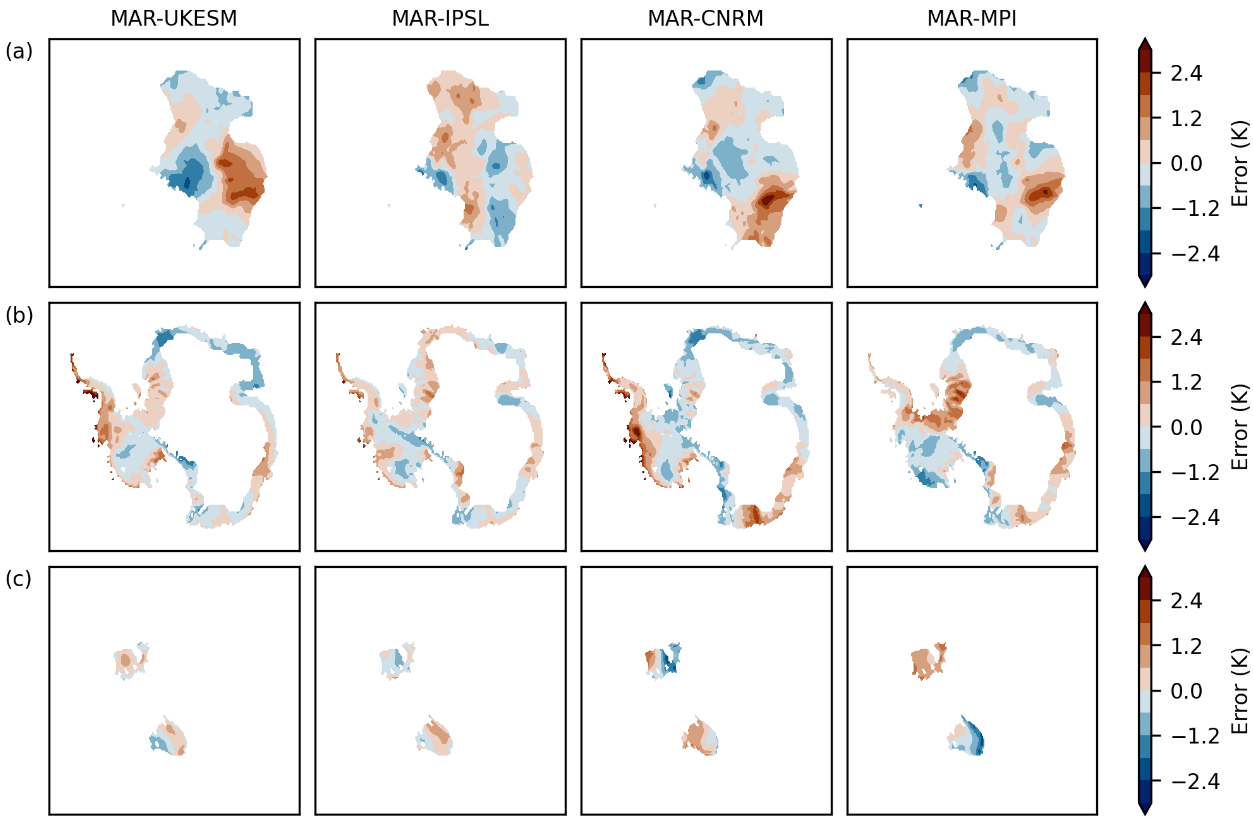


**Figure S8.** Residuals of the linear regression predictions for continental changes in inversion strength. Maps show the errors in the predicted 21st-century change in July potential temperature deficit ($\Delta D_\theta$) based on the mean present-day July static stability ($N^2$) from the full non-cross-validated regressions calculated using all available data. Results for the (a) plateau, (b) escarpment, and (c) Ronne and Ross Ice Shelves are depicted by downscaled GCM.

**Table S9.** Model performance indicators for linear regression models predicting the 21st-century change in July potential temperature deficit ($\Delta D_\theta$) from present-day July static stability ($N^2$). Data are shown by the number of clusters in the spatial cross-validation and for the regressions trained on the full datasets. MAE is mean absolute error and MedAE is median absolute error. PL represents plateau, ES represents escarpment, and IS represents the Ronne and Ross Ice Shelves.

| Model | Region | Clusters | MAE (K) | MedAE (K) | Model | Region | Clusters | MAE (K) | MedAE (K) |
|---|---|---|---|---|---|---|---|---|---|
| MAR-UKESM | PL | 3 | 0.78 | 0.72 | MAR-IPSL | PL | 3 | 0.57 | 0.52 |
| | | 5 | 0.72 | 0.73 | | | 5 | 0.53 | 0.49 |
| | | 7 | 0.70 | 0.65 | | | 7 | 0.52 | 0.48 |
| | | Full | 0.63 | 0.48 | | | Full | 0.50 | 0.43 |
| | ES | 3 | 0.67 | 0.60 | | ES | 3 | 0.42 | 0.35 |
| | | 5 | 0.64 | 0.53 | | | 5 | 0.46 | 0.38 |
| | | 7 | 0.63 | 0.54 | | | 7 | 0.43 | 0.36 |
| | | Full | 0.54 | 0.39 | | | Full | 0.43 | 0.36 |
| | IS | 4 | 0.43 | 0.39 | | IS | 4 | 0.43 | 0.35 |
| | | 6 | 0.45 | 0.44 | | | 6 | 0.42 | 0.37 |
| | | 8 | 0.44 | 0.43 | | | 8 | 0.38 | 0.36 |
| | | Full | 0.40 | 0.36 | | | Full | 0.36 | 0.30 |
| MAR-CNRM | PL | 3 | 0.70 | 0.67 | MAR-MPI | PL | 3 | 0.55 | 0.46 |
| | | 5 | 0.64 | 0.59 | | | 5 | 0.51 | 0.42 |
| | | 7 | 0.61 | 0.56 | | | 7 | 0.51 | 0.44 |
| | | Full | 0.58 | 0.47 | | | Full | 0.50 | 0.39 |
| | ES | 3 | 0.71 | 0.61 | | ES | 3 | 0.57 | 0.52 |
| | | 5 | 0.74 | 0.64 | | | 5 | 0.58 | 0.52 |
| | | 7 | 0.73 | 0.64 | | | 7 | 0.61 | 0.56 |
| | | Full | 0.66 | 0.54 | | | Full | 0.56 | 0.47 |
| | IS | 4 | 0.96 | 0.93 | | IS | 4 | 1.07 | 0.96 |
| | | 6 | 0.88 | 0.86 | | | 6 | 0.94 | 0.87 |
| | | 8 | 0.86 | 0.88 | | | 8 | 0.94 | 0.90 |
| | | Full | 0.75 | 0.75 | | | Full | 0.79 | 0.74 |

## S6 Supplementary material for "Discussion"

**Table S10.** Contribution of the surface temperature inversion to 21st-century near-surface warming at six ice core sites. Sites were selected to approximately capture the Antarctic regions in Stenni et al. (2017).

| Site | Contribution (%) |
|---|---|
| Berkner Island | 9 |
| James Ross | 36 |
| East Dronning Maud Land | 17 |
| EPICA Dome C | 29 |
| WAIS Divide | 10 |
| TALDICE | 8 |

## S7 CMIP6 references

In this section, we have included the sources of the publicly available CMIP6 data we use throughout the analysis. References are formatted as required by CMIP6 citation guidelines. The CMIP6 data are licensed under the Creative Commons Attribution 4.0 International (CC BY 4.0) license, accessible at https://creativecommons.org/licenses/by/4.0/. The only changes made to the CMIP6 data were data cleaning steps.

### S7.1 Historical data


- Tang, Yongming; Rumbold, Steve; Ellis, Rich; Kelley, Douglas; Mulcahy, Jane; Sellar, Alistair; Walton, Jeremy; Jones, Colin (2019): *MOHC UKESM1.0-LL model output prepared for CMIP6 CMIP historical*. Version *20190406*. Earth System Grid Federation. https://doi.org/10.22033/ESGF/CMIP6.6113

- Tang, Yongming; Rumbold, Steve; Ellis, Rich; Kelley, Douglas; Mulcahy, Jane; Sellar, Alistair; Walton, Jeremy; Jones, Colin (2019): *MOHC UKESM1.0-LL model output prepared for CMIP6 CMIP historical*. Version *20200309*. Earth System Grid Federation. https://doi.org/10.22033/ESGF/CMIP6.6113

- Boucher, Olivier; Denvil, Sébastien; Levavasseur, Guillaume; Cozic, Anne; Caubel, Arnaud; Foujols, Marie-Alice; Meurdesoif, Yann; Cadule, Patricia; Devilliers, Marion; Ghattas, Josefine; Lebas, Nicolas; Lurton, Thibaut; Mellul, Lidia; Musat, Ionela; Mignot, Juliette; Cheruy, Frédérique (2018): *IPSL IPSL-CM6A-LR model output prepared for CMIP6 CMIP historical*. Version *20180803*. Earth System Grid Federation. https://doi.org/10.22033/ESGF/CMIP6.5195

- Voldoire, Aurore (2018): *CMIP6 simulations of the CNRM-CERFACS based on CNRM-CM6-1 model for CMIP experiment historical*. Version *20180917*. Earth System Grid Federation. https://doi.org/10.22033/ESGF/CMIP6.4066

- Jungclaus, Johann; Bittner, Matthias; Wieners, Karl-Hermann; Wachsmann, Fabian; Schupfner, Martin; Legutke, Stephanie; Giorgetta, Marco; Reick, Christian; Gayler, Veronika; Haak, Helmuth; de Vrese, Philipp; Raddatz, Thomas; Esch, Monika; Mauritsen, Thorsten; von Storch, Jin-Song; Behrens, Jörg; Brovkin, Victor; Claussen, Martin; Crueger, Traute; Fast, Irina; Fiedler, Stephanie; Hagemann, Stefan; Hohenegger, Cathy; Jahns, Thomas; Kloster, Silvia; Kinne, Stefan; Lasslop, Gitta; Kornblueh, Luis; Marotzke, Jochem; Matei, Daniela; Meraner, Katharina; Mikolajewicz, Uwe; Modali, Kameswarrao; Müller, Wolfgang; Nabel, Julia; Notz, Dirk; Peters-von Gehlen, Karsten; Pincus, Robert; Pohlmann, Holger; Pongratz, Julia; Rast, Sebastian; Schmidt, Hauke; Schnur, Reiner; Schulzweida, Uwe; Six, Katharina; Stevens, Bjorn; Voigt, Aiko; Roeckner, Erich (2019): *MPI-M MPI-ESM1.2-HR model output prepared for CMIP6 CMIP historical*. Version *20190710*. Earth System Grid Federation. https://doi.org/10.22033/ESGF/CMIP6.6594


### S7.2 Future data


- Good, Peter; Sellar, Alistair; Tang, Yongming; Rumbold, Steve; Ellis, Rich; Kelley, Douglas; Kuhlbrodt, Till (2019): *MOHC UKESM1.0-LL model output prepared for CMIP6 ScenarioMIP ssp585*. Version *20190507*. Earth System Grid Federation. https://doi.org/10.22033/ESGF/CMIP6.6405

- Good, Peter; Sellar, Alistair; Tang, Yongming; Rumbold, Steve; Ellis, Rich; Kelley, Douglas; Kuhlbrodt, Till (2019): *MOHC UKESM1.0-LL model output prepared for CMIP6 ScenarioMIP ssp585*. Version *20200415*. Earth System Grid Federation. https://doi.org/10.22033/ESGF/CMIP6.6405

- Boucher, Olivier; Denvil, Sébastien; Levavasseur, Guillaume; Cozic, Anne; Caubel, Arnaud; Foujols, Marie-Alice; Meurdesoif, Yann; Cadule, Patricia; Devilliers, Marion; Dupont, Eliott; Lurton, Thibaut (2019): *IPSL IPSL-CM6A-LR model output prepared for CMIP6 ScenarioMIP ssp585*. Version *20190903*. Earth System Grid Federation. https://doi.org/10.22033/ESGF/CMIP6.5271

- Voldoire, Aurore (2019): *CNRM-CERFACS CNRM-CM6-1 model output prepared for CMIP6 ScenarioMIP ssp585*. Version *20190219*. Earth System Grid Federation. https://doi.org/10.22033/ESGF/CMIP6.4224

– Schupfner, Martin; Wieners, Karl-Hermann; Wachsmann, Fabian; Steger, Christian; Bittner, Matthias; Jungclaus, Johann; Früh, Barbara; Pankatz, Klaus; Giorgetta, Marco; Reick, Christian; Legutke, Stephanie; Esch, Monika; Gayler, Veronika; Haak, Helmuth; de Vrese, Philipp; Raddatz, Thomas; Mauritsen, Thorsten; von Storch, Jin-Song; Behrens, Jörg; Brovkin, Victor; Claussen, Martin; Crueger, Traute; Fast, Irina; Fiedler, Stephanie; Hagemann, Stefan; Hohenegger, Cathy; Jahns, Thomas; Kloster, Silvia; Kinne, Stefan; Lasslop, Gitta; Kornblueh, Luis; Marotzke, Jochem; Matei, Daniela; Meraner, Katharina; Mikolajewicz, Uwe; Modali, Kameswarrao; Müller, Wolfgang; Nabel, Julia; Notz, Dirk; Peters-von Gehlen, Karsten; Pincus, Robert; Pohlmann, Holger; Pongratz, Julia; Rast, Sebastian; Schmidt, Hauke; Schnur, Reiner; Schulzweida, Uwe; Six, Katharina; Stevens, Bjorn; Voigt, Aiko; Roeckner, Erich (2019): *DKRZ MPI-ESM1.2-HR model output prepared for CMIP6 ScenarioMIP ssp585*. Version *20190710*. Earth System Grid Federation. https://doi.org/10.22033/ESGF/CMIP6.4403

### S7.3 Additional data for UKESM cell area

– Tang, Yongming; Rumbold, Steve; Ellis, Rich; Kelley, Douglas; Mulcahy, Jane; Sellar, Alistair; Walton, Jeremy; Jones, Colin (2019): *MOHC UKESM1.0-LL model output prepared for CMIP6 CMIP piControl*. Version *20190705*. Earth System Grid Federation. https://doi.org/10.22033/ESGF/CMIP6.6298

## References


Bahn, V. and McGill, B. J.: Testing the predictive performance of distribution models, Oikos, 122, 321–331, https://doi.org/10.1111/j.1600-0706.2012.00299.x, 2013.

Roberts, D. R., Bahn, V., Ciuti, S., Boyce, M. S., Elith, J., Guillera-Arroita, G., Hauenstein, S., Lahoz-Monfort, J. J., Schröder, B., Thuiller, W., Warton, D. I., Wintle, B. A., Hartig, F., and Dormann, C. F.: Cross-validation strategies for data with temporal, spatial, hierarchical, or phylogenetic structure, Ecography, 40, 913–929, https://doi.org/10.1111/ecog.02881, 2017.

Stenni, B., Curran, M. A. J., Abram, N. J., Orsi, A., Goursaud, S., Masson-Delmotte, V., Neukom, R., Goosse, H., Divine, D., van Ommen, T., Steig, E. J., Dixon, D. A., Thomas, E. R., Bertler, N. A. N., Isaksson, E., Ekaykin, A., Werner, M., and Frezzotti, M.: Antarctic climate variability on regional and continental scales over the last 2000 years, Clim. Past, 13, 1609–1634, https://doi.org/10.5194/cp-13-1609-2017, 2017.

Sun, K., Hu, Y., Lakhanpal, G., and Zhou, R. Z.: Spatial cross-validation for GeoAI, in: Handbook of Geospatial Artificial Intelligence, edited by: Gao, S., Hu, Y., and Li, W., CRC Press, 1 edn., 201–214, https://doi.org/10.1201/9781003308423-10, 2023.

Valavi, R., Elith, J., Lahoz-Monfort, J. J., and Guillera-Arroita, G.: blockCV: An r package for generating spatially or environmentally separated folds for k-fold cross-validation of species distribution models, Methods Ecol. Evol., 10, 225–232, https://doi.org/10.1111/2041-210X.13107, 2019.